Noname manuscript No.
(will be inserted by the editor)

Supplementary Material for "Digital Volume Correlation Challenge 2.0: A Comprehensive Dataset for Digital Volume Correlation Benchmarking"

Zixiang Tong [1] · Yujie Zhang [1] · Edward Andò [2] · Bin Chen [3] · Brendan P. Croom [4] · John O. Dabiri [5] · Christian Franck [6] · Matthew K. Fu [5] · Helena Jin [7] · Orion L. Kafka [8,9] · Sriram Kunnoth [10,11,12] · Thao D. Nguyen [13,17] · Jacob Notbohm [6] · Mohak Patel [14] · Mainak Sarkar [6,15] · Angkur J. Shaikeea [5] · Jing Zhang [6] · Alexander K. Landauer [8†] · Jin Yang [1,16*]

Received: date / Accepted: date

[1]Department of Aerospace Engineering and Engineering Mechanics, The University of Texas at Austin, USA

[2]EPFL Center for Imaging, École Polytechnique Fédérale de Lausanne (EPFL), Switzerland

[3]Wallenberg Wood Science Center, Department of Fiber and Polymer Technology, KTH Royal Institute of Technology, Sweden

[4]Research and Exploratory Development Department, Johns Hopkins Applied Physics Laboratory, USA

[5]Division of Engineering and Applied Science, California Institute of Technology, USA

[6]Department of Mechanical Engineering, University of Wisconsin-Madison, USA

[7]Sandia National Laboratory, USA

[8]Material Measurement Laboratory, National Institute of Standards and Technology, USA

[9]Currently: QuesTek Innovations, USA

[10]Department of Applied Mechanics, Indian Institute of Technology Delhi, India

[11]Division of Clinical Medicine, School of Medicine and Population Health, The University of Sheffield, UK

[12]Insigneo Institute, The University of Sheffield, UK

[13]Department of Mechanical Engineering, Johns Hopkins University, USA

[14]Google DeepMind, USA

[15]Carl R. Woese Institute for Genomic Biology, University of Illinois Urbana-Champaign, USA

[16]Texas Materials Institute, The University of Texas at Austin, USA

[17]The Wilmer Eye Institute, Johns Hopkins School of Medicine, USA

[†]Co-corresponding author; E-mail: alexander.landauer@nist.gov

[*]Corresponding author; E-mail: jin.yang@austin.utexas.edu

S1 Autocorrelation Function Computation and Interpretation

S1.1 Computation of the Autocorrelation Function

We computed 3D spatial autocorrelation functions for all datasets to quantify characteristic structural length scales and spatial continuity. The following procedure was applied consistently across all volumes.

For a discrete 3D image $I(x, y, z)$, the autocorrelation function is defined as

$$R(\boldsymbol{r}) = \sum_{x,y,z} I(x, y, z)\, I(x + \Delta_x,\, y + \Delta_y,\, z + \Delta_z), \tag{S1}$$

where $\boldsymbol{r} = [\Delta_x, \Delta_y, \Delta_z]^\top$ denotes the spatial displacement. The zero-lag position $\boldsymbol{r} = [0, 0, 0]^\top$ corresponds to perfect overlap and yields the maximum correlation value. This formulation provides a direct measure of the characteristic texture scale encoded in the image. For comparison across datasets, the autocorrelation was normalized by its zero-lag value:

$$\tilde{R}(\boldsymbol{r}) = \frac{R(\boldsymbol{r})}{R(\mathbf{0})}, \tag{S2}$$

which is equivalent to the normalized cross-correlation of the image with itself.

Autocorrelation was computed using the `match_template` function from `scikit-image`, which performs normalized cross-correlation via FFT-based convolution [1]. All computations were carried out on selected subvolumes within each 3D dataset. Based on feature-scale RVE analysis, each 3D region of interest (ROI) was chosen to ensure statistical convergence of local texture properties.

To avoid wrap-around artifacts inherent to FFT-based convolution and to enable full displacement evaluation, each ROI was extended via zero padding. This approach prevents artificial periodicity, preserves physical interpretation outside the image domain, and ensures numerical stability. Because convolution is defined as:

$$(f * g)(r) = \sum_{x} f(x)\, g(r - x), \tag{S3}$$

where the kernel $g(\bullet)$ is flipped relative to the definition of correlation. Therefore, the `match_template` implementation internally flips the template along all axes so that the resulting FFT-based computation matches the mathematical definition of correlation.

The output of the 3D autocorrelation computation is a volumetric function whose coordinates represent the displacement of the shifted template (in our case, the original unpadded 3D ROI). Each voxel value in this volume corresponds to the normalized correlation coefficient at that displacement. To convert this 3D volume into a 1D radial autocorrelation curve, we computed the Euclidean displacement

magnitude

$$|\boldsymbol{r}| = \sqrt{\Delta_x^2 + \Delta_y^2 + \Delta_z^2}, \tag{S4}$$

for every voxel in the autocorrelation map. Because $|\boldsymbol{r}|$ is a continuous quantity, it was discretized using

$$r_{\text{bin}} = \text{floor}(|\boldsymbol{r}|), \tag{S5}$$

which assigns each voxel to the largest integer not exceeding its true displacement. For each integer displacement k, all autocorrelation values satisfying "$k \leq |\boldsymbol{r}| < k + 1$" were averaged to obtain the radial autocorrelation value $\tilde{R}(k)$. The standard deviation of the same set was also computed. Adding and subtracting this standard deviation from the mean yields an uncertainty interval that reflects the variability of correlation values across each spherical shell, thereby indicating the degree of directional dependence at that spatial scale.

S1.2 Guide to Interpreting Autocorrelation Curves

In addition to the computational details above, this section provides a visual and conceptual guide for interpreting the shapes and statistics of autocorrelation ($\overline{AC}$) curves. Figure S1 illustrates how key properties of the material's microstructure, namely feature size (coarseness), directional dependence, and quasi-periodicity, are manifested in the shape and statistics of the $\overline{AC}$ function.

The primary characteristics to consider when analyzing an $\overline{AC}$ curve are:

i) **Autocorrelation length and feature coarseness:** The autocorrelation length quantifies the characteristic size, or coarseness, of features within an image. As illustrated in Fig. S1(a), this single parameter effectively captures the visual difference between microstructures. Images containing fine features are characterized by a short autocorrelation length, while images with larger, coarser features correspond to a long autocorrelation length.

ii) **Directional dependence:** The degree of directional dependence is assessed by examining the statistical deviation (e.g., plus/minus one standard deviation) of the $\overline{AC}$ function calculated along different directions. As shown in Fig S1(b), if the features are statistically similar in all directions, the $\overline{AC}$ curves will be very similar, resulting in a tight, narrow deviation band. If the features exhibit strong directional dependence (i.e., they have a preferential orientation or shape), the $\overline{AC}$ curves will vary significantly with direction, leading to a broad deviation band (see Fig. S1(c)).

iii) **Quasi-periodicity:** The presence of repeating or quasi-periodic structures within the image volume introduces characteristic oscillations in the $\overline{AC}$ curve, as illustrated in Fig. S1(d). The locations

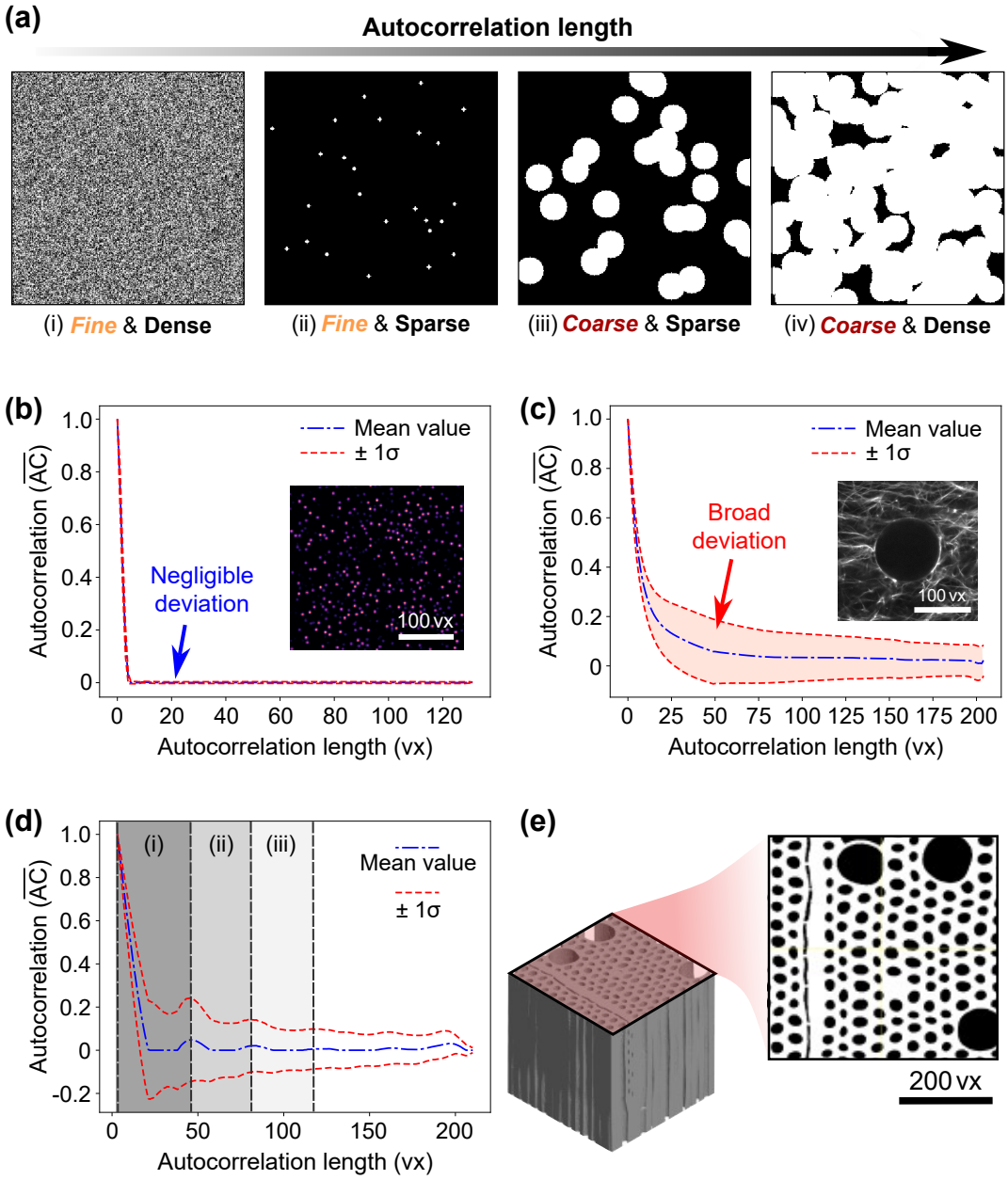

Fig. S1: Conceptual illustration for interpreting autocorrelation ($\overline{AC}$) curves. (a) Representative image textures with increasing characteristic feature size, from fine to coarse and from sparse to dense, illustrating how spatial structure influences $\overline{AC}$ behavior. (b) $\overline{AC}$ curve for a fine and statistically isotropic texture, showing rapid decay with negligible directional deviation (narrow $\pm 1\sigma$ band). (c) Conversely, $\overline{AC}$ curve for a structured or anisotropic texture exhibiting a broader $\pm 1\sigma$ band, indicating increased directional dependence and spatial heterogeneity. (d) Oscillatory patterns in the $\overline{AC}$ curve are a strong indicator of quasi-periodicity, suggesting the presence of repeating structural elements within the image. (e) Example of a real microstructure with heterogeneous, multi-scale features, illustrating how complex spatial organization can lead to mixed $\overline{AC}$ characteristics (see (d)), including long correlation tails and local periodicity.

of the peaks and valleys in the curve can provide quantitative information about the spacing and arrangement of these repeating features.

As shown in Fig. S1(e), in realistic materials, heterogeneous and multi-scale microstructures often exhibit a combination of these behaviors, including mixed feature sizes, long correlation tails, and partial periodicity. This highlights that $\overline{AC}$-based metrics capture both local feature characteristics and larger-scale structural organization.

S2 Full Evolution of ROI-Specific Autocorrelation Functions (ACFs)

This section presents the complete evolution of the radial autocorrelation functions (ACFs) computed across concentric ROIs for each dataset analyzed in this study. Each dataset is represented by one composite figure that includes (i) the ROI footprints on the mid–z slice and (ii) the full family of $\overline{AC}(r)$ curves across increasing ROI sizes. Thresholds at "$\overline{AC} = 1/\mathrm{e}$", "$\overline{AC} = 0.10$", and "$\overline{AC} = 0.01$" are marked to indicate the feature-scale, mesoscale, and far-tail correlation regimes, respectively.

S2.1 ROI Construction and Increment Strategy

For each dataset, the ROI center was randomly selected from locations with sufficient surrounding volume to allow progressive expansion without exceeding dataset boundaries. ROIs were defined as concentric cubic volumes and expanded in fixed increments of Δr pixels, starting from a small initial edge length. The initial length and increment size were chosen empirically to ensure adequate sampling of small-scale correlations while maintaining computational efficiency. All parameter values used for each dataset are documented in the supporting repository.

No interpolation was applied when determining threshold-crossing distances; correlation lengths were evaluated directly from the discrete radial sampling of $\overline{AC}(r)$. Accordingly, the reported representative volume element (RVE) sizes represent discrete approximations subject to voxel resolution.

S2.2 Definition of Correlation-Length Convergence and RVE Criteria

The RVE at each correlation threshold was determined using a quantitative convergence criterion based on a sliding-window coefficient of variation (CV). Let $\{L_i\}$ denote the sequence of extracted correlation lengths ordered by increasing ROI effective size. A sliding window of $w = 4$ voxels consecutive measurements $\{L_{i-w+1}, \ldots, L_i\}$ was considered stabilized when

$$\mathrm{CV}_i = \frac{\sigma(L_{i-w+1}, \ldots, L_i)}{\mu(L_{i-w+1}, \ldots, L_i)} \leq \varepsilon, \tag{S6}$$

where $\sigma(\bullet)$ and $\mu(\bullet)$ denote the sample standard deviation and mean over the window, respectively; ε is a prescribed dimensionless tolerance on the relative variation of $\{L_i\}$ within the window. Different tolerance values ε were adopted for different correlation regimes to reflect their distinct statistical variability: $\varepsilon = 0.05$ for the feature-scale ($\overline{AC} = 1/\mathrm{e}$), $\varepsilon = 0.10$ for the mesoscale regime ($\overline{AC} = 0.10$), and $\varepsilon = 0.20$ for the far-tail regime ($\overline{AC} = 0.01$).

Stability was additionally required to persist across all subsequent windows (persistence check), reducing the likelihood of falsely identifying transient plateaus as convergence and ensuring robustness with respect to increasing observation volume.

To guard against overly strict rejection when characteristic lengths are inherently small (e.g., $L < 5$ voxels), where minor numerical noise can disproportionately inflate the CV, an absolute tolerance fallback is applied in parallel: a window is also considered stable if

$$\sigma_L \leq \delta, \tag{S7}$$

where $\delta = 0.5$ voxels applies uniformly across all regimes. The stabilization criterion is therefore met when *either* condition holds:

$$\mathrm{CV}_i \leq \varepsilon \quad \text{or} \quad \sigma_L \leq \delta. \tag{S8}$$

The progressively relaxed tolerances account for increased statistical fluctuation and finite-volume sensitivity at larger correlation distances. The smallest ROI satisfying the stabilization criterion defines the RVE for the corresponding regime.

S2.3 Summary of Extracted RVE Sizes

Table S1 reports the feature-scale ($\overline{AC} = 1/\mathrm{e}$) and mesoscale ($\overline{AC} = 0.1$) RVEs extracted for all analyzed datasets, expressed as the minimal stabilized cubic ROI size $[H, W, D]$ in voxel units. Dataset names follow the official naming convention of the NIST PDR data bundle, and the section column indicates where each dataset is introduced in the main manuscript. Entries marked "N/A" indicate that the stabilization criterion defined above was not satisfied within the finite ROI sequence tested for that dataset. For most datasets, the maximum tested ROI remains well below the full image extent, so an "N/A" entry reflects an incomplete sampling of the convergence trajectory rather than a physical bound on the correlation length. This is most common in the mesoscale column, where longer correlation lengths would require extending the ROI sequence further to capture stabilization.

Several trends emerge from the table. First, the reported RVEs span more than an order of magnitude, from 6–20 voxels for statistically dense and uniform datasets to 200–240 voxels for datasets whose native features occupy comparably large spatial scales. The smallest RVEs are concentrated among most DVC Challenge 1.0 groups, the synthetic beads (Patel and Yang), the Yang hydrogel, and the Fu swimming-animal datasets (Shrimp S1, Shrimp S2, and Jellyfish), where densely distributed features yield rapidly decaying and statistically well-sampled autocorrelation functions. The largest RVEs occur in wood samples (Chen Balsa: $[240, 240, 240]$ voxels at the feature scale; Chen Spruce: $[200, 200, 200]$ voxels), whose native cellular structures and growth-ring spacings are themselves large relative to the imaging resolution, and in open-cell foams such as Sriram Foam S3 ($[200, 200, 200]$ voxels), whose individual pore cells span comparable spatial scales.

Second, the mesoscale RVE is, in most cases, equal to or *smaller* than the feature-scale RVE. Although this may initially appear counterintuitive, given that the correlation length at $\overline{AC} = 0.10$ voxels is intrinsically longer than at $\overline{AC} = 1/\mathrm{e}$ voxels and one would expect longer lengths to demand larger ROIs to stabilize, the observed pattern reflects the progressively relaxed CV tolerance used at longer length scales ($\varepsilon = 0.10$ for the mesoscale vs. $\varepsilon = 0.05$ for the feature scale). The two-fold looser tolerance empirically compensates for the approximately 1.5–2-fold increase in correlation length between the two regimes, allowing the mesoscale estimate to stabilize at smaller ROIs than the feature-scale estimate. Third, when the z component of the RVE equals the dataset's z-extent, as in Notbohm Fibrous S1 ($[120, 120, 101]$ voxels (vx), where "$z = 101$ vx" coincides with the full dataset depth), that value represents a truncated upper bound rather than a converged estimate, and only the in-plane (x, y) dimensions reflect genuine stabilization. Finally, the four remaining "N/A" entries, all in the mesoscale column (SPAM Concrete S2, Franck Polyacrylamide, Notbohm Fibrous S2, and Shaikeea Polymer), indicate that the extracted $L_{0.10}$ length estimate did not stabilize within the tested ROI range. In each of these cases, the

autocorrelation itself does cross the 0.10 threshold; what fails is the convergence of $L_{0.10}$ as the ROI is progressively enlarged, and the underlying mechanisms differ across datasets. In the Shaikeea Polymer dataset, the Kelvin-lattice unit cell is comparable in size to the ROI increment used here, so $L_{0.10}$ oscillates quasi-periodically with ROI size and fails to settle below the CV tolerance. In SPAM Concrete S2, Franck Polyacrylamide, and Notbohm Fibrous S2, the $L_{0.10}$ trajectory remains non-stationary within the tested range. A plausible explanation is that the underlying mesoscale structure governing $L_{0.10}$ in these datasets is of comparable or larger size than the largest tested ROI, so each ROI captures only a local, non-representative portion of the mesoscale correlation and $L_{0.10}$ has not yet formed a statistically stable estimate; direct verification would require extending the ROI sequence beyond the range sampled here. In all cases, a markedly larger ROI sequence would likely be required to resolve the mesoscale RVE.

Due to the large number of analyzed datasets, the complete ROI-dependent ACF evolution plots, extracted correlation-length trajectories, and detailed convergence reports are not reproduced here. The supporting repository provides the configuration files and analysis scripts used to generate these outputs, enabling full reproducibility of the figures and results presented in this work.

Table S1: Extracted representative volume elements (RVEs) at the feature-scale ($\overline{AC} = 1/e$) and mesoscale ($\overline{AC} = 0.10$) thresholds, reported as stabilized cubic ROI sizes $[H, W, D]$ in voxel units.

Dataset	**Section**	**Feature RVE (unit: vx)**	**Mesoscale RVE (unit: vx)**
DVC1 S1	3.1.1	[20, 20, 20]	[20, 20, 20]
DVC1 S2	3.1.1	[34, 34, 35]	[20, 20, 20]
DVC1 S3	3.1.1	[50, 50, 50]	[20, 20, 20]
DVC1 S4	3.1.1	[20, 20, 20]	[20, 20, 20]
DVC1 S5a	3.1.1	[20, 20, 20]	[20, 20, 20]
DVC1 S5b	3.1.1	[20, 20, 20]	[20, 20, 20]
DVC1 S6	3.1.1	[60, 60, 60]	[40, 40, 40]
Landauer Foam	3.1.2	[40, 40, 40]	[40, 40, 40]
Sriram Foam S1	3.1.3	[110, 110, 110]	[80, 80, 80]
Sriram Foam S2	3.1.3	[110, 110, 110]	[80, 80, 80]
Sriram Foam S3	3.1.3	[200, 200, 200]	[140, 140, 140]
Chen Balsa	3.1.4	[240, 240, 240]	[160, 160, 160]
Chen Birch S1	3.1.4	[70, 70, 70]	[40, 40, 40]
Chen Birch S2	3.1.4	[70, 70, 70]	[40, 40, 40]
Chen Spruce	3.1.4	[200, 200, 200]	[80, 80, 80]
SPAM Sandstone	3.1.5	[20, 20, 20]	[35, 35, 35]
SPAM Soil	3.1.5	[55, 55, 55]	[40, 40, 40]
SPAM Concrete S1	3.1.5	[40, 40, 40]	[40, 40, 40]
SPAM Concrete S2	3.1.5	[15, 15, 15]	N/A
SPAM Concrete S3	3.1.5	[75, 75, 75]	[75, 75, 75]
SPAM Sand S1	3.1.5	[100, 100, 100]	[60, 60, 60]
SPAM Sand S2	3.1.5	[140, 140, 140]	[40, 40, 40]
Kafka Polymer S1	3.1.6	[120, 120, 120]	[80, 80, 80]
Kafka Polymer S2	3.1.6	[100, 100, 100]	[80, 80, 80]
Shaikeea Polymer	3.1.7	[100, 100, 100]	N/A
Patel Beads	3.2.1	[20, 20, 20]	[20, 20, 20]
Yang Beads S1	3.2.1	[18, 18, 18]	[12, 12, 12]
Yang Beads S2	3.2.1	[18, 18, 18]	[18, 18, 18]
Yang Beads S3	3.2.1	[12, 12, 12]	[12, 12, 12]
Franck Polyacrylamide	3.2.2	[16, 16, 16]	N/A
Yang Hydrogel	3.2.3	[12, 12, 12]	[6, 6, 6]
Notbohm Fibrous S2	3.2.4	[20, 20, 20]	N/A
Notbohm Fibrous S1	3.2.5	[120, 120, 101]	[100, 100, 100]
Nguyen Lamina Cribrosa	3.2.6	[95, 95, 95]	[70, 70, 70]
Fu Shrimp S1	3.3.1	[20, 20, 20]	[20, 20, 20]
Fu Shrimp S2	3.3.1	[30, 30, 30]	[30, 30, 30]
Fu Jellyfish	3.3.1	[20, 20, 20]	[20, 20, 20]

S3 Dataset-Specific Autocorrelation Analyses

This section presents the dataset-specific autocorrelation analysis results for all datasets described in the main manuscript. Each figure shows the angularly averaged radial autocorrelation function $\overline{AC}(r)$ and its ± 1 standard deviation envelope for the reference volumetric image of the corresponding dataset. The characteristic correlation lengths at the 1/e and 0.10 thresholds are indicated, quantifying the feature-scale and mesoscale spatial organization, respectively. For a detailed description of the autocorrelation methodology and interpretation, the reader is referred to Section 2.4 of the main manuscript and Section S1 of this Supplementary Material.

S3.1 Micro X-ray and Neutron Computed Tomography

Figure S2 shows the autocorrelation analysis for the DVC Challenge 1.0 Dataset S4 (syntactic foam). The mean autocorrelation function decreases monotonically with increasing spatial separation, with characteristic lengths of approximately 2.2 vx at the 1/e threshold and 4.2 vx at the 10 % threshold. The narrow standard deviation band indicates low directional variability in the spatial texture, consistent with the randomly distributed hollow glass microballoons embedded in the elastomer matrix.

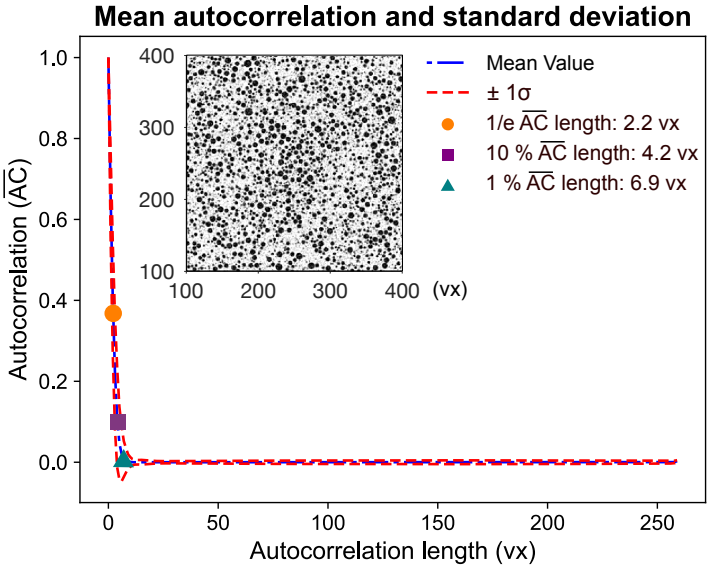

Fig. S2: Autocorrelation analysis of the reference volumetric image for syntactic foam rigid body motion (DVC Challenge 1.0 Dataset XCT S4 [2]). [Dataset corresponds to Section 3.1.1 of the main manuscript.]

Figure S3 presents the autocorrelation analysis for the elastomeric polymer foam reference volume. The 1/e, 10 %, and 1 % $\overline{AC}$ lengths are 2.3 vx, 5.0 vx, and 12.5 vx, respectively. The rapid initial

decay reflects the fine-scale, interconnected pore structure of the foam, while the narrow deviation band indicates minimal directional dependence in the spatial texture.

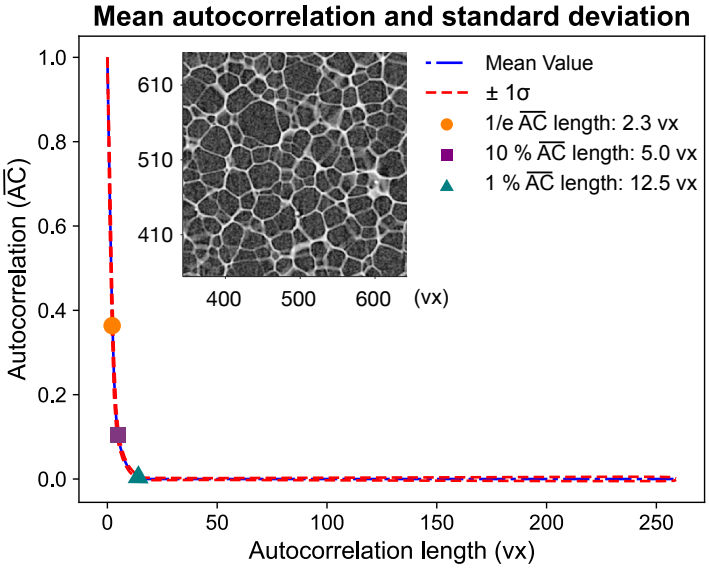

Fig. S3: Autocorrelation analysis of the reference volumetric image for the elastomeric polymer foam under uniaxial compression [3]. [Dataset corresponds to Section 3.1.2 of the main manuscript.]

Figure S4 shows the autocorrelation analysis for the open-cell foam reference volume (Sriram Foam S1). The slow decay of the mean autocorrelation curve reflects the large structural elements (thick struts and large voids) of the reticulated microstructure, yielding a 10 % $\overline{AC}$ length of approximately 34.8 vx. Despite the structural sparseness, the narrow standard deviation band indicates that the microstructure exhibits minimal directional dependence.

Figure S5 compares the autocorrelation functions for the three numerically generated wood microstructures. Balsa exhibits the slowest decay, yielding the largest characteristic feature size (10 % $\overline{AC}$ length of 42.5 vx), reflecting its large cell lumens. Birch (S1) shows the most rapid initial decay (10 % $\overline{AC}$ length of 15.1 vx), consistent with its finer fibers. Spruce is intermediate (10 % $\overline{AC}$ length of 22.1 vx) with weaker quasi-periodic features. All three species exhibit wide standard deviation bands, confirming the expected strong directional dependence of wood microstructures along the longitudinal fiber direction.

The prominent oscillations in the Birch curve reflect the regular, repeating pattern of fibers and vessels characteristic of many hardwoods. Spruce, a softwood, shows a much weaker quasi-periodic signature, while Balsa's curve is nearly monotonic, suggesting a less ordered cellular arrangement. These quantitative metrics provide direct guidelines for DVC analysis setup: the characteristic feature size in-

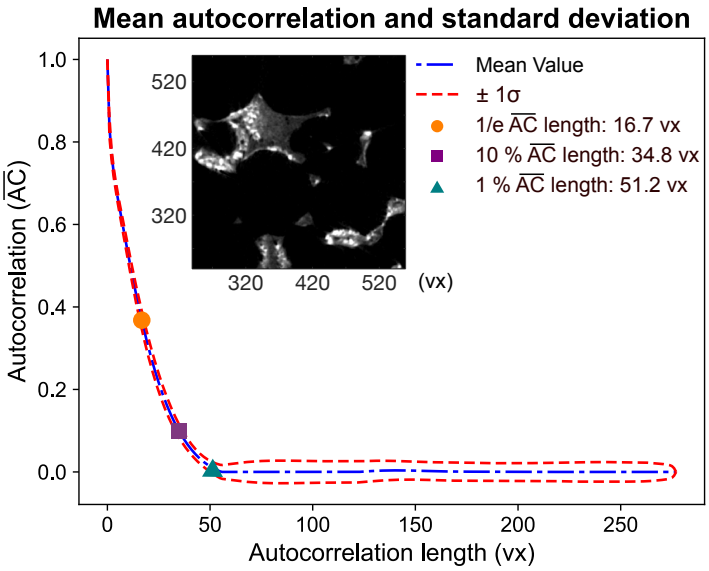

Fig. S4: Autocorrelation analysis of the reference volumetric image for the open-cell foam (Sriram Foam S1). The narrow standard deviation band indicates minimal directional dependence in the microstructure. [Dataset corresponds to Section 3.1.3 of the main manuscript.]

forms optimal subset selection, where the larger and more random features in Balsa would necessitate a larger subset to ensure robust tracking compared to the finer, more quasi-periodic structure of Birch.

Figure S6 presents the autocorrelation analysis for the SPAM "Sand" dataset, comparing XCT (Sand S1) and neutron computed tomography (NCT) (Sand S2) images of the same specimen. The two imaging modalities produce distinct correlation decay profiles: the XCT image emphasizes the solid granular framework, while the NCT image is more sensitive to fluid-phase contrast. Characteristic feature sizes and standard deviation bands differ between modalities, illustrating how imaging physics influences autocorrelation-based feature characterization.

Figure S7 shows the autocorrelation analysis for the vat photo-polymer built metamaterial in the transverse build orientation (Kafka Polymer S1). The relatively slow decay of the $\overline{AC}$ curve reflects the large-scale repeating lattice architecture of the triply periodic minimal surface (TPMS) structure, with a 1/e correlation length of 9.5 vx and a 10 % length of 25.0 vx.

Figure S8 presents the autocorrelation analysis for the open-cell Kelvin lattice polymeric specimen. The repeating lattice architecture produces oscillatory features in the $\overline{AC}$ curve, reflecting the quasi-periodic unit-cell structure of the lattice. The 1/e correlation length is approximately 0.8 vx.

S3.2 Laser-Scanning Optical Microscopy

Figure S9 shows the autocorrelation analysis for the synthetic fluorescence bead volume. The rapid initial decay, with a 1/e correlation length of approximately 2.2 vx, reflects the small size of the individual beads.

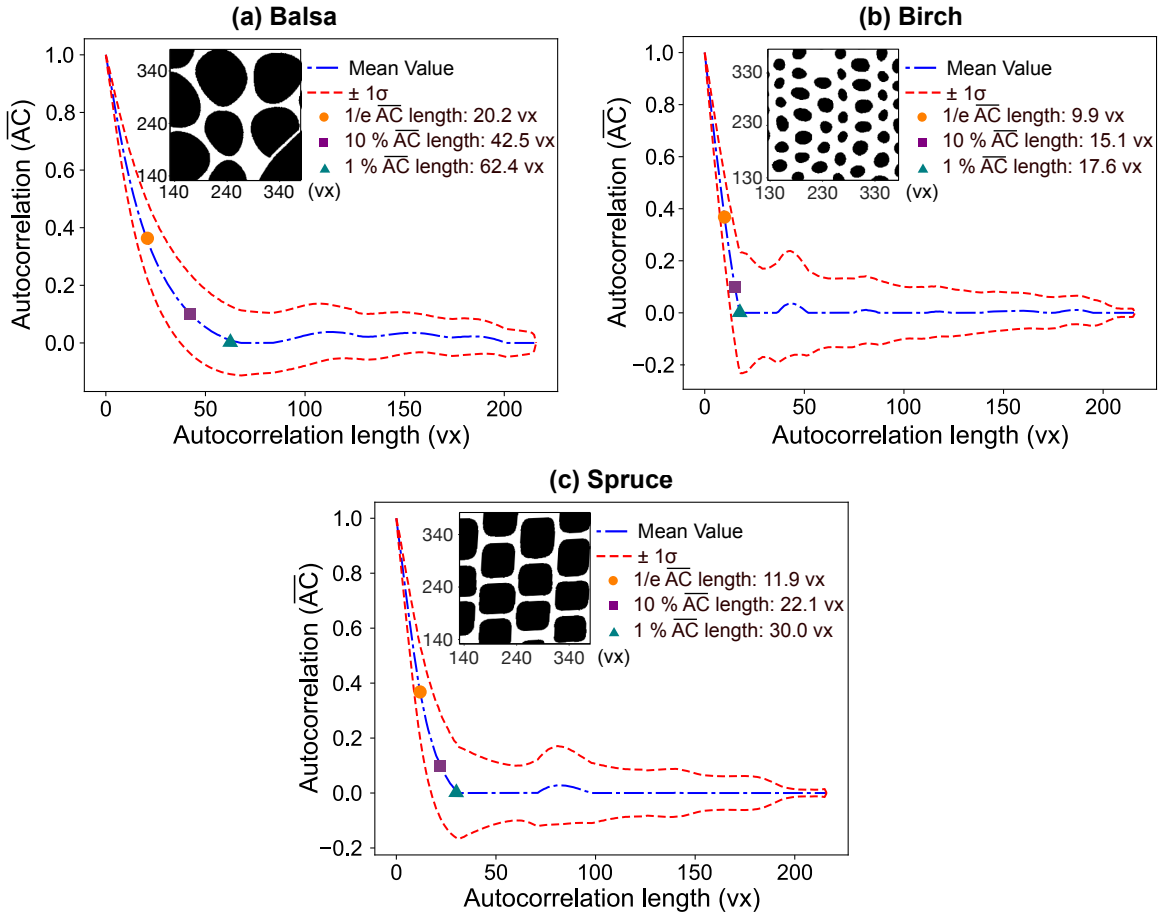

Fig. S5: Autocorrelation analysis for the three wood microstructures: (a) Balsa, (b) Birch (S1), and (c) Spruce. The solid blue line represents the mean $\overline{AC}$, while the dashed lines indicate ±1 standard deviation. Oscillations in the Birch curve indicate quasi-periodic organization in the cellular structure. [Dataset corresponds to Section 3.1.4 of the main manuscript.]

The narrow deviation band indicates a spatially uniform bead distribution with negligible directional dependence, generated by Poisson-disc sampling.

Figure S10 presents the autocorrelation analysis for the experimental polyacrylamide (PAAm) hydrogel uniaxial tension dataset. The feature-scale and mesoscale $\overline{AC}$ lengths are 1.7 vx and 8.0 vx, respectively. The correlation decay is characteristic of densely embedded fluorescent microparticles imaged by multiphoton microscopy.

Figure S11 shows the autocorrelation analysis for the PAAm hydrogel under sphere indentation. The embedded fluorescent beads produce a well-defined bead-scale correlation decay, with characteristic lengths comparable to those of other confocal microscopy datasets in this collection.

Figure S12 presents the autocorrelation analysis for the synthetic collagen fiber network. The 1/e correlation length of 2.9 vx reflects the thin fiber diameter, while the substantially larger mesoscale

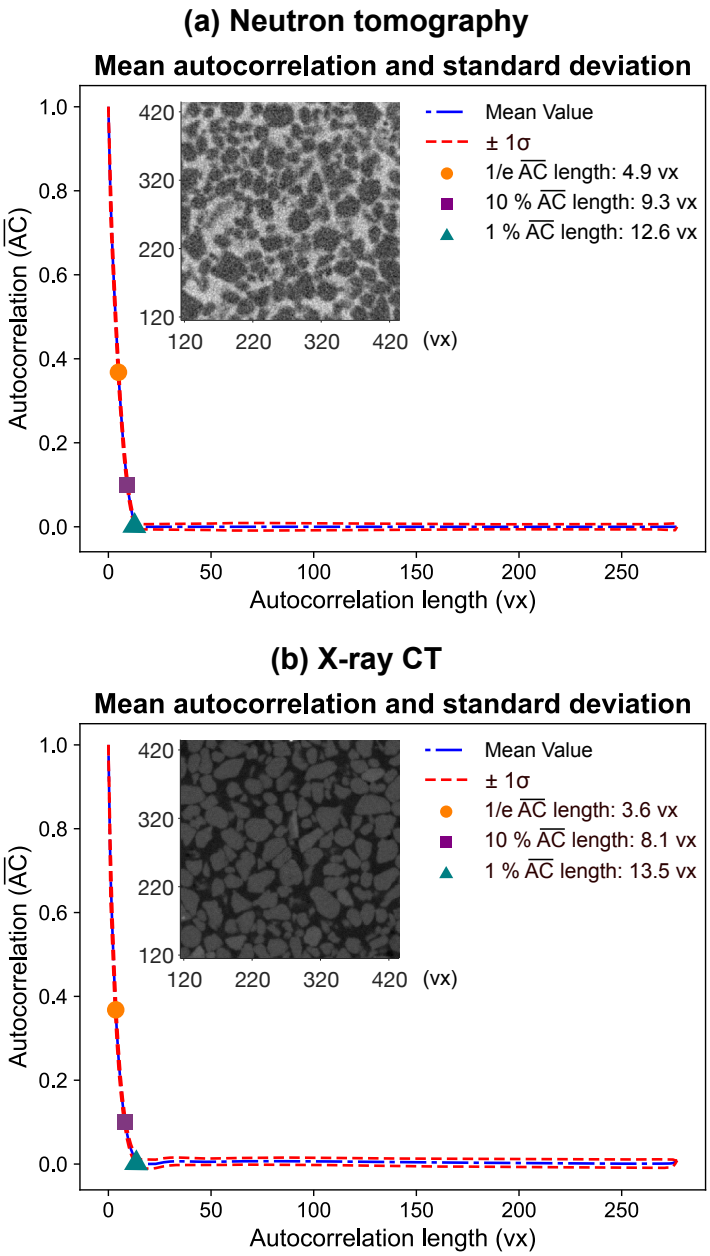

Fig. S6: Autocorrelation analysis of the reference volumetric image for SPAM 04 "SandNX" dataset: (a) XCT image; (b) NCT image. [Dataset corresponds to Section 3.1.5 of the main manuscript.]

length (10 % $\overline{AC}$ = 29.0 vx) captures the inter-fiber spacing and network mesh size. The relatively wide deviation band reflects the inherent directional dependence of the randomly assembled fiber architecture.

Figure S13 shows the autocorrelation analysis for the experimental collagen network with a contracting hydrogel inclusion. Compared to the corresponding synthetic collagen dataset, the deviation band is notably wider. This increased directional variability arises because the number of z-planes collected was substantially smaller than the in-plane dimensions, a deliberate choice to reduce image acquisition time given the spherically symmetric boundary condition. The 1 % autocorrelation length is not reported here

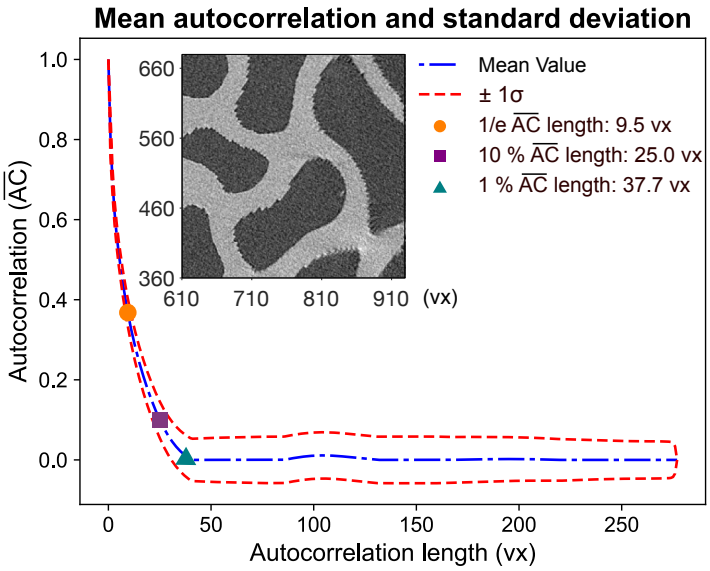

Fig. S7: Autocorrelation analysis of the reference volumetric image for the vat photo-polymer built metamaterial (Kafka Polymer S1). [Dataset corresponds to Section 3.1.6 of the main manuscript.]

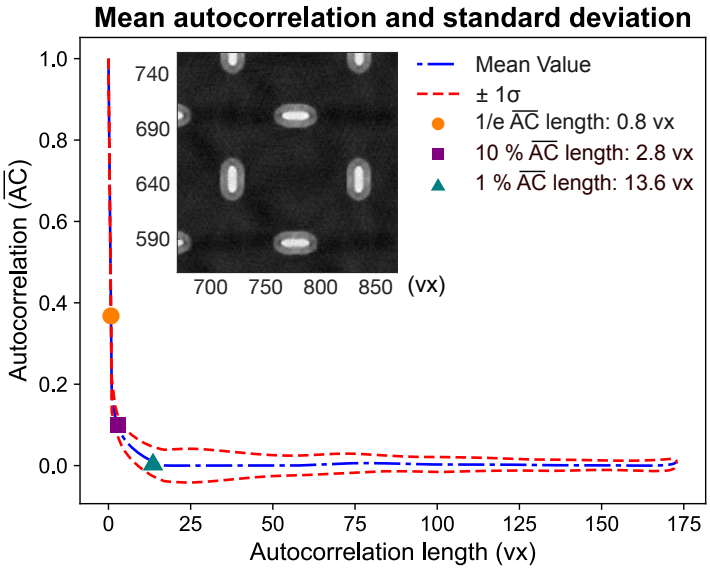

Fig. S8: Autocorrelation analysis of the reference volumetric image for the polymeric specimens with an open-cell Kelvin lattice structure. [Dataset corresponds to Section 3.1.7 of the main manuscript.]

because the correlation curve does not reach this threshold within the available spatial range, reflecting the presence of long-range structural correlations in the dataset.

Figure S14 presents the autocorrelation analysis for the human lamina cribrosa second harmonic generation (SHG) reference image (Run_02). The 1/e and 10 % correlation lengths are 11.4 vx and 24.6 vx, respectively, reflecting the characteristic collagen beam dimensions within the laminar network. The relatively wide deviation band is consistent with the preferential orientation of collagen beams within the lamina cribrosa.

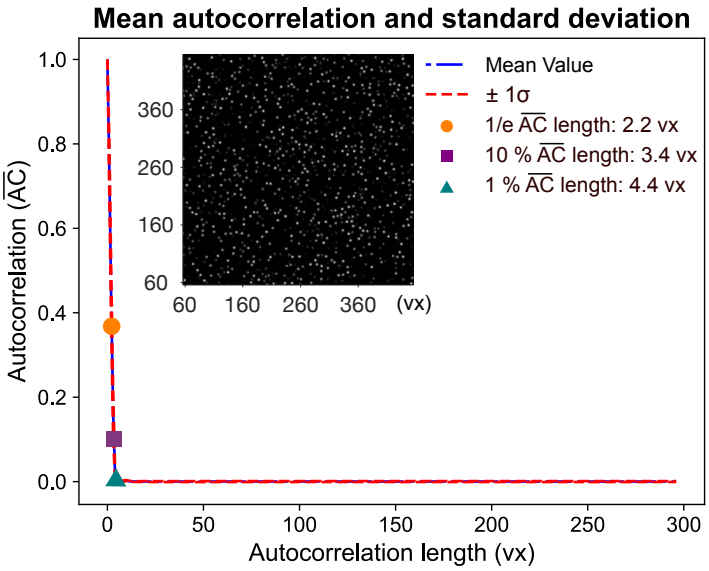

Fig. S9: Autocorrelation analysis of the reference volumetric image incorporating synthetic fluorescence beads. [Dataset corresponds to Section 3.2.1 (Set #1) of the main manuscript.]

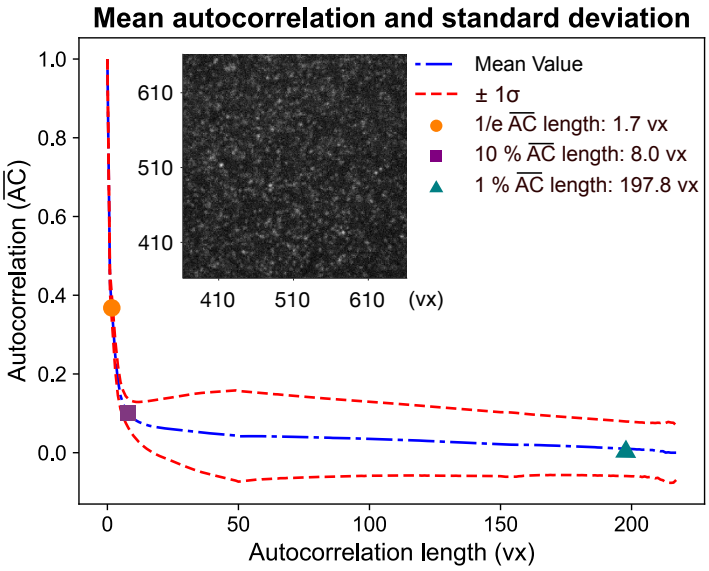

Fig. S10: Autocorrelation analysis of the reference volumetric image for the PAAm hydrogel uniaxial tension dataset. [Dataset corresponds to Section 3.2.2 of the main manuscript.]

S3.3 Other Methods

Figures S15 and S16 present the autocorrelation analyses for the two swimming animal datasets acquired using Scanning Particle Image Velocimetry. The brine shrimp dataset, Fu Shrimp S1, (Fig. S15) exhibits a very short 1/e correlation length of approximately 1.3 vx, reflecting the small tracer particle size relative to the voxel resolution. The jellyfish dataset (Fig. S16) shows an even shorter correlation length of 0.8 vx, due to the coarser voxel resolution (105 µm) used to capture the larger imaging volume.

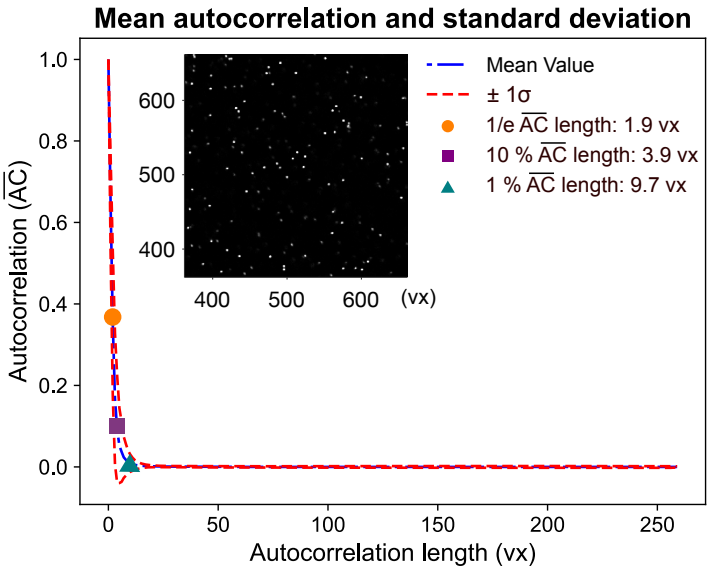

Fig. S11: Autocorrelation analysis of the reference volumetric image for the polyacrylamide hydrogel under sphere indentation. [Dataset corresponds to Section 3.2.3 of the main manuscript.]

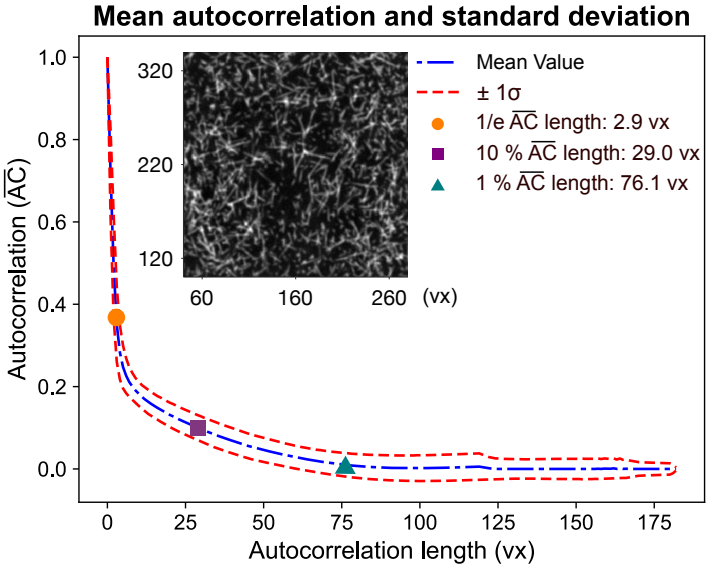

Fig. S12: Autocorrelation analysis of the reference volumetric image for the synthetic collagen fiber network. [Dataset corresponds to Section 3.2.4 of the main manuscript.]

Figure S17 shows the autocorrelation analysis for the synthetic magma compression dataset from the Collaborative Computational Project in Tomographic Imaging (CCPi) repository. The correlation decay quantifies the characteristic structural length scales of the synthetically generated porous material, providing a reference for evaluating DVC algorithms on this class of volcanic-origin microstructures.

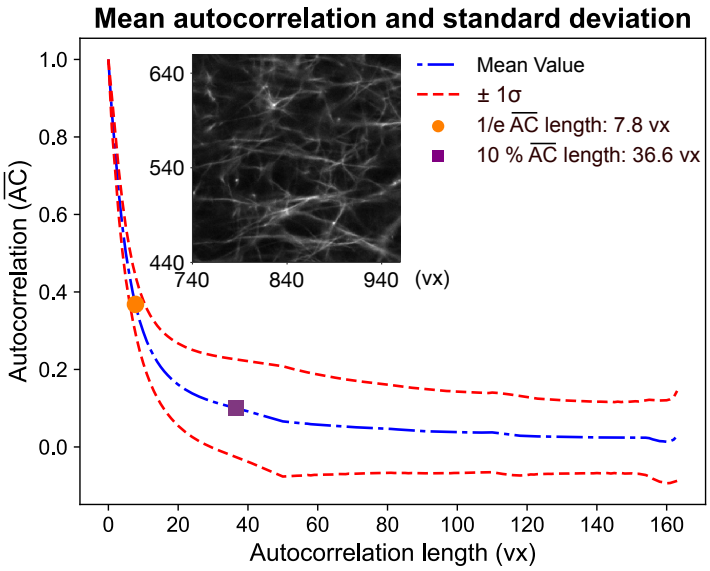

Fig. S13: Autocorrelation analysis of the reference volumetric image for the collagen network with contracting hydrogel inclusion. [Dataset corresponds to Section 3.2.5 of the main manuscript.]

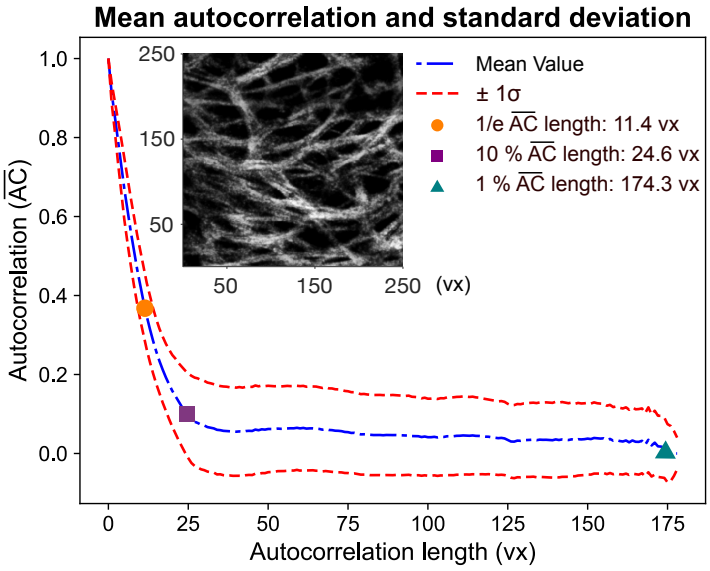

Fig. S14: Autocorrelation analysis of the SHG reference image from "`Run_02`" (HLC-0430-LE-05mmHg-set2-decon-3DCL.tif) for the human lamina cribrosa dataset. [Dataset corresponds to Section 3.2.6 of the main manuscript.]

S4 Additional Publicly Available Volumetric Imaging Datasets

Beyond the datasets presented in the main manuscript and analyzed in the preceding sections, several publicly available volumetric imaging datasets from other imaging modalities may also be suitable for DVC algorithm development and validation. This section briefly surveys relevant datasets from optical coherence tomography (OCT) and magnetic resonance imaging (MRI).

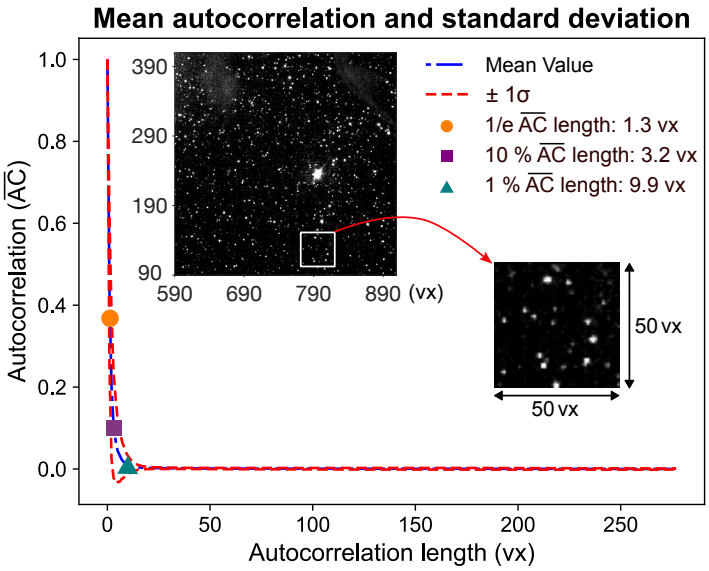

Fig. S15: Autocorrelation analysis of the reference volumetric image for the flow field surrounding swimming shrimp (Fu Shrimp S1). [Dataset corresponds to Section 3.3.1 of the main manuscript.]

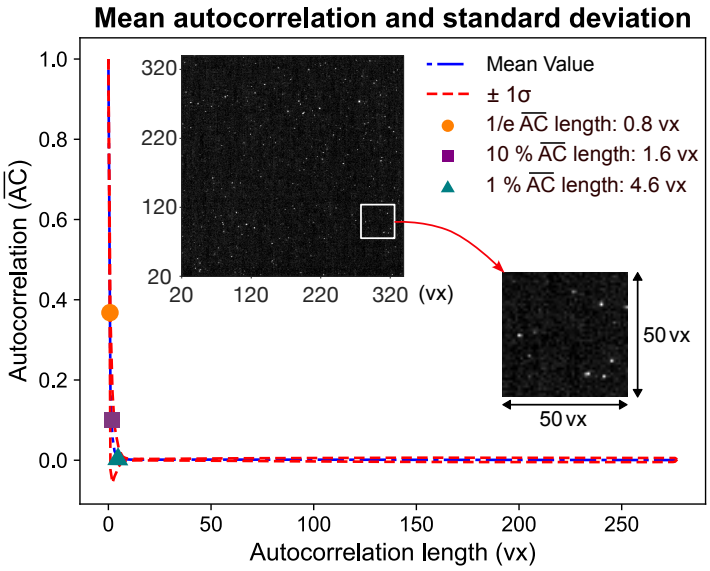

Fig. S16: Autocorrelation analysis of the reference volumetric image for the flow field surrounding jellyfish. [Dataset corresponds to Section 3.3.1 of the main manuscript.]

S4.1 Optical Coherence Tomography (OCT) and Optical Coherence Tomography Angiography (OCTA)

Optical Coherence Tomography (OCT) is a noninvasive imaging modality widely used for acquiring high-resolution three-dimensional images of biological tissues [4]. OCT produces volumetric image stacks by scanning a focused light beam across a sample and reconstructing depth-resolved backscattered signals. The resulting images typically consist of a series of cross-sectional slices (B-scans) that are assembled into volumetric datasets.

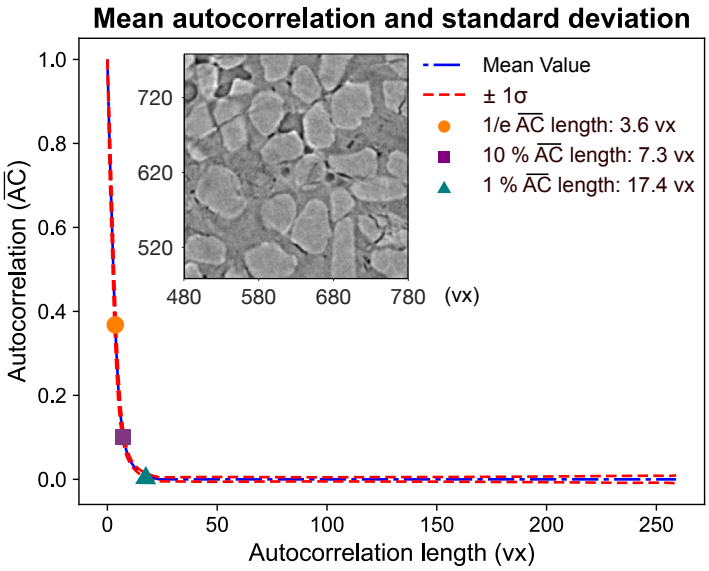

Fig. S17: Autocorrelation analysis of the reference volumetric image for the synthetic magma dataset. [Dataset corresponds to Section 3.3.2 of the main manuscript.]

Building upon OCT technology, optical coherence tomography angiography (OCTA) has been developed as a new useful imaging modality for providing functional information on retinal blood vessels and microvascular structures. OCTA detects temporal variations in the amplitude or phase of backscattered light to generate volumetric angiographic images without the need for exogenous contrast agents [5]. The resulting OCTA volumes can be projected across different retinal layers to separately visualize the vascular plexuses within the retina.

Although OCT and OCTA datasets are primarily developed for medical image segmentation, disease diagnosis, and ophthalmic research, the volumetric speckle patterns and structural textures present in OCT/OCTA images provide natural feature carriers suitable for correlation-based displacement tracking. Consequently, such datasets may serve as useful benchmarks for evaluating Digital Volume Correlation (DVC) algorithms in biological imaging applications, including studies of tissue deformation, biomechanics, and optical coherence elastography.

Several publicly available OCT and OCTA datasets provide volumetric images that may be suitable for DVC algorithm development and validation. For example, (i) the OCTAVE dataset (`https://zenodo.org/records/14580071`) [6] provides 3D OCT volumes with pixel-level annotations of retinal structures and pathological features. A related dataset reported by Huang et al. [7] contains 224 volumetric OCT images annotated with pigment epithelial detachment and intraretinal fluid. Both these two datasets include cases of age-related macular degeneration (AMD) and diabetic macular edema (DME). (ii) The OCTA-500 dataset (`https://ieee-dataport.org/open-access/octa-500`) contains OCT and OCTA imaging volumes from 500 subjects acquired under two different fields of view [8]. The dataset

includes multimodal volumetric images together with extensive annotations, including demographic information, retinal layer segmentation, vascular segmentation, and foveal avascular zone labeling. (iii) The GAMMA dataset (`https://huggingface.co/datasets/ctmedtech/GAMMA`) is a multimodal glaucoma grading dataset that pairs two-dimensional color fundus photographs with three-dimensional OCT volumes. Released as part of the GAMMA challenge (`https://gamma.grand-challenge.org/`), the dataset was designed to support the development of algorithms that integrate information from both OCT and fundus imaging for automated glaucoma diagnosis. (iv) Additional volumetric OCT datasets are available for preclinical imaging studies. For instance, the Murine OCT volume dataset (`https://data.bris.ac.uk/data/dataset/ypfrg4sz8jwi2ehjqjubbq526`) contains high-resolution three-dimensional OCT scans of mouse eyes, acquired as a series of 512 B-scans centered on the optic nerve head.

In general, OCT and OCTA datasets consist of volumetric image stacks with dimensions on the order of several hundred pixels in each direction and voxel resolutions in the micrometer range, making them well suited for high-resolution volumetric image analysis and correlation-based displacement measurements.

S4.2 Magnetic Resonance Imaging (MRI)

Magnetic Resonance Imaging (MRI) is another widely used noninvasive imaging modality capable of producing high-resolution three-dimensional volumetric images of biological tissues. MRI volumes are typically reconstructed from multiple slices acquired using magnetic resonance signal encoding and are commonly stored in volumetric formats such as NIfTI or DICOM. Compared with optical imaging methods, MRI offers excellent soft-tissue contrast and the ability to image deep structures within biological systems.

Although MRI datasets are primarily developed for clinical diagnosis, medical image segmentation, and machine learning applications, the volumetric anatomical textures present in MRI images can provide suitable features for volumetric image correlation techniques. While MRI provides volumetric images with defined voxel spacing that enable quantitative spatial measurements, geometric distortions arising from gradient nonlinearity and field inhomogeneity can affect absolute dimensional accuracy. Modern correction techniques significantly reduce these effects; however, for DVC applications requiring high-precision displacement measurements, MRI data may exhibit lower geometric fidelity compared to X-ray CT or optical imaging modalities. Nonetheless, MRI datasets may still serve as valuable benchmarks for evaluating DVC algorithms in biomedical imaging contexts, including studies of organ deformation, tissue biomechanics, and medical image registration.

Several large-scale open-access MRI datasets are available to the research community. For example, (i) the Human Connectome Project (HCP) (`https://www.humanconnectome.org/`) provides high-resolution structural MRI volumes from approximately 1200 subjects, including T1-weighted and T2-weighted scans with isotropic resolutions as fine as 0.7 mm. Typical reconstructed volumes are approximately $320 \times 320 \times 256$ voxels, making this dataset particularly suitable for structural brain analysis, image registration, and volumetric modeling. (ii) The Alzheimer's Disease Neuroimaging Initiative (ADNI) dataset (`https://adni.loni.usc.edu/`) contains longitudinal MRI volumes from more than 2000 subjects, together with complementary imaging modalities such as positron emission tomography (PET) scans. The MRI volumes typically have approximately 1 mm isotropic resolution and are widely used for studying neurodegenerative disease progression and longitudinal anatomical changes. (iii) The Brain Tumor Segmentation (BraTS) dataset (`https://www.med.upenn.edu/cbica/brats/`) provides multi-modal MRI volumes for brain tumor analysis, including T1, contrast-enhanced T1 (T1c), T2, and fluid-attenuated inversion recovery (FLAIR) images. The dataset includes imaging data from thousands of patients and is commonly used for tumor segmentation and machine learning studies. Typical volumetric image sizes are approximately $240 \times 240 \times 155$ voxels. (iv) Another commonly used open dataset is the IXI dataset (`https://brain-development.org/ixi-dataset/`), which contains MRI volumes from approximately 600 healthy subjects acquired using T1-, T2-, and proton-density-weighted imaging sequences. These datasets are widely used for brain morphology studies, image registration benchmarking, and neuroimaging research. (v) The fastMRI dataset (`https://fastmri.med.nyu.edu/`), released by NYU and Facebook AI Research, provides large collections of MRI scans together with raw k-space data used for MRI reconstruction research. The dataset contains both brain and knee MRI volumes and is widely used for developing reconstruction algorithms and machine learning methods. (vi) Additional open MRI datasets include the Open Access Series of Imaging Studies (OASIS) (`https://sites.wustl.edu/oasisbrains/`), which contains longitudinal T1-weighted MRI volumes for studies of brain aging. The dataset includes approximately 1000 subjects and has been widely used for neurodegeneration research.

Beyond brain imaging datasets, several open MRI datasets focus on other anatomical structures. For example, the MRNet dataset (`https://stanfordmlgroup.github.io/competitions/mrnet/`) provides three-dimensional knee MRI volumes from more than 1300 patients and is commonly used for musculoskeletal imaging research. Large-scale population, non-open-source imaging datasets are also available, such as the UK Biobank imaging dataset (`https://www.ukbiobank.ac.uk/`), which contains MRI scans from more than 100,000 participants, including brain, cardiac, and body MRI volumes. Access to the UK Biobank dataset typically requires a research application and approval process.

S5 Evaluation of DVC Bias and Noise Floor Across Imaging Modalities

In this study, the corresponding displacement errors in each direction (x, y, and z) are defined as the differences between the measured and reference (ground-truth or zero-motion) displacements. These component-wise errors are used to quantify both systematic bias and random uncertainty. The systematic bias is defined as the ensemble-averaged error with respect to the reference displacement, while the uncertainty (noise floor) is quantified by the standard deviation of the zero-mean fluctuations.

To obtain a scalar measure of the overall displacement error, we compute the displacement error magnitude as the Euclidean norm of the three components:

$$|\mathbf{u}| = \sqrt{u_x^2 + u_y^2 + u_z^2}. \tag{S9}$$

Because the displacement components are subject to measurement uncertainty, the magnitude $|\boldsymbol{u}|$ is also a random variable. Assuming that the displacement errors in the three directions are statistically independent, with means μ_x, μ_y, μ_z and standard deviations $\sigma_x, \sigma_y, \sigma_z$, the expected squared magnitude can be written as:

$$\mathbb{E}[|\mathbf{u}|^2] = (\mu_x^2 + \sigma_x^2) + (\mu_y^2 + \sigma_y^2) + (\mu_z^2 + \sigma_z^2). \tag{S10}$$

Using a second-order uncertainty propagation based on Taylor expansion (delta method) approximation [9, 10], the mean displacement magnitude is estimated as:

$$\mu_{|\boldsymbol{u}|} \approx \sqrt{\mu_x^2 + \mu_y^2 + \mu_z^2 + \sigma_x^2 + \sigma_y^2 + \sigma_z^2}. \tag{S11}$$

Similarly, the variance of the displacement magnitude can be approximated via error propagation:

$$\mathrm{Var}(|\mathbf{u}|) \approx \frac{\mu_x^2\sigma_x^2 + \mu_y^2\sigma_y^2 + \mu_z^2\sigma_z^2}{\mu_{|\boldsymbol{u}|}^2}, \tag{S12}$$

which yields the standard deviation:

$$\sigma_{|\mathbf{u}|} \approx \sqrt{\frac{\mu_x^2\sigma_x^2 + \mu_y^2\sigma_y^2 + \mu_z^2\sigma_z^2}{\mu_{|\mathbf{u}|}^2}}. \tag{S13}$$

References

1. S. Van der Walt, J. L. Schönberger, J. Nunez-Iglesias, F. Boulogne, J. D. Warner, N. Yager, E. Gouillart, and T. Yu. scikit-image: image processing in Python. *PeerJ*, 2:e453, 2014. doi:10.7717/peerj.453.
2. B. P. Croom, D. Burden, H. Jin, N. H. Vonk, J. P. M. Hoefnagels, B. Smaniotto, F. Hild, E. Quintana, Q. Sun, X. Nie, et al. Interlaboratory study of digital volume correlation error due to X-ray computed tomography equipment and scan parameters: an update from the DVC challenge. *Experimental Mechanics*, 61:395–410, 2021. doi:10.1007/s11340-020-00653-x.
3. A. K. Landauer, O. L. Kafka, N. H. Moser, and A. M. Forster. A materials dataset for elastomeric foam impact mitigating materials. 2022. doi:10.18126/6h74-leb4.
4. A. Rozhyna, G. M. Somfai, M. Atzori, D. C. DeBuc, A. Saad, J. Zoellin, and H. Müller. Exploring publicly accessible optical coherence tomography datasets: a comprehensive overview. *Diagnostics*, 14(15):1668, 2024. doi:10.3390/diagnostics14151668.
5. A. H. Kashani, C. L. Chen, J. K. Gahm, F. Zheng, G. M. Richter, P. J. Rosenfeld, Y. Shi, and R. K. Wang. Optical coherence tomography angiography: a comprehensive review of current methods and clinical applications. *Progress in Retinal and Eye Research*, 60:66–100, 2017. doi:10.1016/j.preteyeres.2017.07.002.
6. D. S. Kermany, W. Poon, A. Bawiskar, N. Nehra, O. Davarci, G. Das, M. Vasquez, S. Schaal, R. Raghunathan, and S. T.C. Wong. Identifying retinal features using a self-configuring CNN for clinical intervention. *Investigative Ophthalmology & Visual Science*, 66(6):55–55, 2025. doi:10.1167/iovs.66.6.55.
7. W. Huang, L. Qin, M. Xu, H. Zheng, Y. Gan, S. Pei, R. Wu, Y. Liu, J. Zhong, and G. Ni. Comprehensive 3D optical coherence tomography dataset for AMD and DME: Facilitating deep-learning-based 3D segmentation. *Scientific Data*, 13(1):224, 2026. doi:10.1038/s41597-025-06497-1.
8. M. Li, K. Huang, Q. Xu, J. Yang, Y. Zhang, Z. Ji, K. Xie, S. Yuan, Q. Liu, and Q. Chen. OCTA-500: a retinal dataset for optical coherence tomography angiography study. *Medical Image Analysis*, 93: 103092, 2024. doi:10.1016/j.media.2024.103092.
9. P. R. Bevington and D. K. Robinson. *Data reduction and error analysis*, volume 3. McGraw-Hill New York, 2003.
10. G. Casella and R. Berger. *Statistical inference (2nd ed.)*. Chapman and Hall/CRC, 2024. doi:10.1201/9781003456285.